crystals

MDPI

Article

Heteroleptic Zn(II) Anilate-Based 3D Coordination Polymer with Luminescent Properties

Pietro Rassu [1], Emilia Crăciun [1,2], Mariangela Oggianu [1], Luca Malfatti [3], Fabio Manna [1,2,*] and Maria Laura Mercuri [1]

[1] Department of Chemical and Geological Sciences, University of Cagliari, I-09042 Monserrato, Italy; p.rassu@studenti.uniss.it (P.R.); e.craciun1@studenti.uniss.it (E.C.); mariangela.oggianu@unica.it (M.O.); mercuri@unica.it (M.L.M.)
[2] MOLTECH-Anjou Laboratory, University of Angers, UMR 6200 CNRS, 49000 Angers, France
[3] Laboratory of Materials Science and Nanotechnology, Department of Engineering, University of Sassari, CR-INSTM, Via Vienna 2, 07100 Sassari, Italy; luca.malfatti@uniss.it
* Correspondence: fabio.manna@unica.it

Abstract

We report the synthesis and photophysical properties of a new crystalline Zn^{II}-based heteroleptic coordination polymer, $Zn_2(trz_2An)(trz)_2$, obtained from the combination of 3,6-N-ditriazolyl-2,5-dihydroxy-1,4-benzoquinone ligand (H_2trz_2An) and 1H-1,2,4-triazole (Htrz). Single-crystal X-ray diffraction reveals the formation of an extended network of Zn-triazole layers pillared by anilate ligands, resulting in an overall three-dimensional connectivity reminiscent of the heavily researched CALF-20(Zn). In contrast to CALF-20, the π-conjugated anilate pillars impart a richer electronic structure, giving rise to ligand-centered excited states and detectable luminescence. Photophysical investigations reveal that the optical response is dominated by the intrinsic photosensitivity of the anilate unit and is further modulated by metal coordination and framework formation. These findings further expand the ever-growing coordination chemistry of trz_2An^{2-} linkers and demonstrate that the combination of π-conjugated anilate ligands with N-donor co-ligands is a promising strategy for the design of light-responsive coordination frameworks and, in this case, the assembly of a new heteroleptic anilate-based coordination framework with luminescent properties.

Keywords: anilates; luminescence; photophysics; reticular chemistry; topology

1. Introduction

Among crystalline materials, coordination polymers (CPs) and metal–organic frameworks (MOFs) offer an unparalleled platform for translating molecular design into emergent solid-state properties. Through the rational selection of metal ions and organic linkers, the structure, dimensionality, porosity, and electronic features can be finely tuned, enabling applications in gas storage and separation, catalysis, sensing, magnetism, and optoelectronics [1–10].

In this context, the construction of heteroleptic frameworks is considered an effective approach to modulate the properties of CPs and MOFs [11–13]. By incorporating two or more chemically distinct ligands within the same architecture, heteroleptic systems offer additional degrees of freedom for the independent modulation of structural, electronic, and functional properties. In particular, the combination of N-donor and O-donor ligands has proven especially effective for directing framework assembly while simultaneously

Academic Editor: Vladimir P. Fedin

Received: 11 June 2026
Revised: 3 July 2026
Accepted: 6 July 2026
Published: 10 July 2026

introducing complementary functionalities [13]. Such an approach is particularly attractive for the development of photoactive materials, where one ligand may primarily dictate the network topology and coordination environment, while a second photosensitive ligand provides the electronic states responsible for light absorption and excited-state processes. Consequently, heteroleptic frameworks constitute a versatile platform for engineering structure–property relationships that are difficult to achieve using a single ligand alone [14].

A particularly successful example of this strategy is represented by CALF-20 [15], a zinc-based heteroleptic framework constructed from Zn–triazole layers pillared by oxalate linkers and formulated [Zn_2(1,2,4-triazolate)$_2$(oxalate)]. Owing to its remarkable hydrothermal stability, facile synthesis, and excellent performance in CO_2 capture, CALF-20 has become a benchmark material for evaluating MOFs for industrial gas separation applications [16–22]. Despite these attractive characteristics, the electronic and optical properties of CALF-20 remain largely limited by the absence of extended π-conjugated building blocks, resulting in a framework that is essentially photophysically inactive.

Inspired by the structural simplicity and robustness of CALF-20, we envisioned that replacing the electronically innocent oxalate linker with a π-conjugated quinone derivative would enable the assembly of frameworks retaining the CALF-20 architecture while exhibiting enhanced electronic tunability and optical functionality [23]. Among the available 3,6-disubstituted-2,5-dihydroxy-1,4-benzoquinone candidates, triazolyl-functionalized anilates are particularly appealing because they integrate the versatile coordination chemistry of anilate ligands with additional N-donor sites capable of participating in framework assembly. Moreover, the conjugated quinoid core of the anilate linker introduces accessible electronic excited states, making these ligands attractive building blocks for the development of photoactive coordination materials. In this context, H_2trz_2An represents an especially promising platform, as it combines structural directionality with an intrinsically rich electronic structure. Furthermore, the presence of non-coordinated nitrogen atoms (N4 sites), together with the electron-donating character of the triazolyl substituents, renders this ligand an appealing platform for multifunctional materials. Such features enable combinations of properties, including luminescence and single-ion magnet (SIM) behavior [24], as well as suitability for CO_2 capture and conversion under both dry and humid conditions [25], and the redox activity characteristic of benzoquinone-derivatives [26].

Despite these advances, the coordination chemistry of trz_2An^{2-}-based systems is still far from being fully explored. In particular, to the best of our knowledge, heteroleptic coordination polymers combining the trz_2An^{2-} ligand with additional N-donor co-ligands have not yet been reported. The incorporation of multiple synergistic N-donor ligands within a single coordination framework may therefore represent an effective strategy to tune both the structural features and the photophysical properties of the resulting materials.

Interestingly, although CALF-20-type isoreticular expansions have been extensively explored in silico through systematic linker substitution strategies, including oxalate replacement by alternative building units, experimental access to such predicted architectures—particularly those incorporating electronically active π-conjugated linkers—remains limited [27,28]. In this context, the insertion of the trz_2An^{2-} linker does not lead to a simple isoreticular analogue of CALF-20 but instead promotes the formation of a new heteroleptic coordination polymer with a distinct structural motif and emergent luminescent properties (Scheme 1).

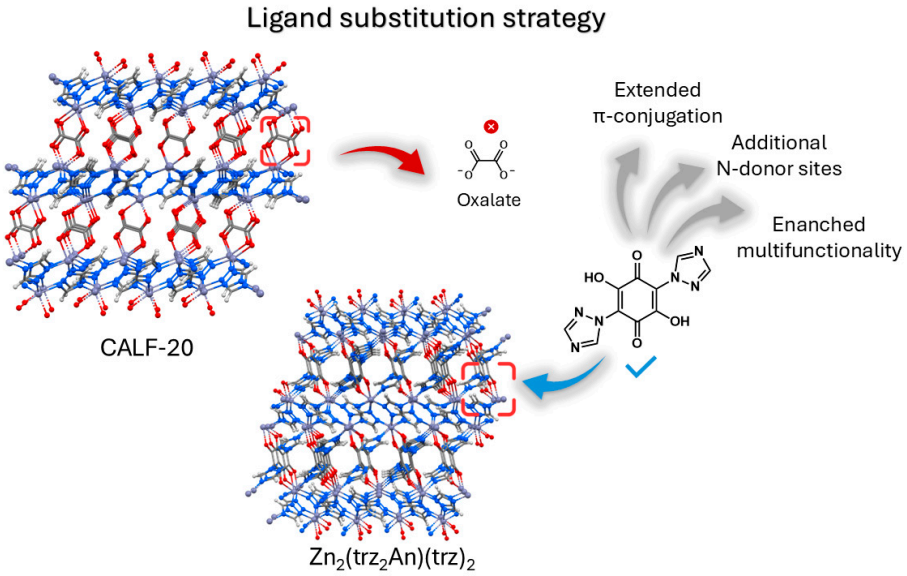

Scheme 1. Engineering photoactivity in CALF-20-type frameworks through anilate linkers.

In this work, we report the synthesis, crystal structure, and photophysical properties of a novel heteroleptic coordination polymer, $Zn_2(trz_2An)(trz)_2$, obtained from the combination of the H_2trz_2An ligands and additional Htrz co-ligands.

2. Materials and Methods

2.1. General Procedure

All starting materials and solvents were purchased from commercial suppliers (Sigma-Aldrich and Zentek (TCI)) and used without further purification. All reactions were performed under ambient laboratory conditions. H_2trz_2An was synthesized according to a procedure reported in the literature [29].

2.2. Synthesis of $Zn_2(trz_2An)(trz)_2$

The synthesis (Figure 1) was performed in a 50 mL stainless steel autoclave. H_2trz_2An (34.3 mg, 0.125 mmol) was dissolved in 6.25 mL Milli-Q water with the addition of NaOH (10 mg, 0.25 mmol) to promote ligand deprotonation. Thus, Htrz (34.5 mg, 0.5 mmol) was added, and the resulting solution was added dropwise to another aqueous $Zn(NO_3)_2$ solution (47.5 mg, 0.25 mmol) prepared in 18.75 mL Milli-Q water. The reaction mixture was sonicated for 5 min, sealed in an autoclave, and then heated at 140 °C for 60 h under hydrothermal conditions. After cooling to room temperature in the autoclave, orange crystals were collected from the mother liquor and washed three times with Milli-Q water over a period of three days by soaking them and changing the solution every day to ensure the removal of potential impurities. The crystals were then collected on filters by vacuum filtration, where they were further washed with a Pasteur pipette three times under Milli-Q water and twice with methanol. They were then air-dried and subjected to analysis (yield: 60%, 32 mg). The reproducibility of the synthesized coordination polymer was evaluated by preparing three independent batches. The resulting materials exhibited consistent structural characteristics and hydrolytic stability (Figure S1) (see the Supplementary Materials).

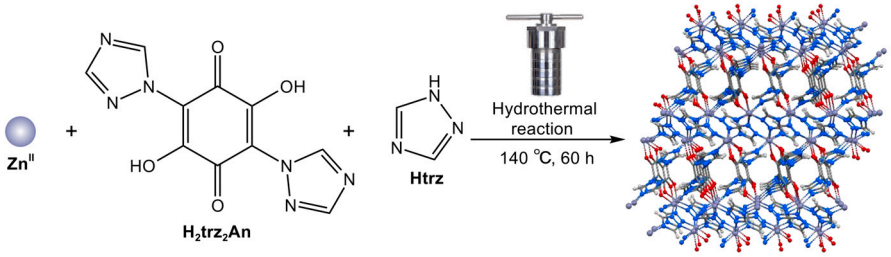

Figure 1. General synthetic procedure to prepare crystalline $Zn_2(trz_2An)(trz)_2$.

2.3. X-Ray Diffraction (Single-Crystal and Powder)

A single crystal of $Zn_2(trz_2An)(trz)_2$ was maintained in contact with the mother liquor and transferred to oil before single-crystal X-ray diffraction (SCXRD) measurement. A suitable crystal was selected and collected at 117 K on a Bruker D8 Venture diffractometer (Mo Kα) equipped with a PHOTON II area detector. The data were indexed and processed with APEX3. Using Olex2 [30], the structure was solved with the SHELXT structure solution program using Intrinsic Phasing and refined with the SHELXL refinement package using least-squares minimization [31,32]. Non-hydrogen atoms were refined anisotropically, and hydrogen atoms were placed in calculated positions, refined using idealized geometries (riding model) and assigned fixed isotropic displacement parameters. A summary of the crystallographic data and the structure refinement is given in Table S1. CCDC: 2560796 contains supplementary crystallographic data for $Zn_2(trz_2An)(trz)_2$.

Powder X-ray diffraction (PXRD) measurements were performed under ambient conditions on a Bruker D8 Advance diffractometer using Cu Kα radiation (40 kV, 40 mA) and a LYNXEYE XE-T detector. Gently ground crystals of the compound were placed on a silicon monocrystal zero-background sample holder. XRD data were collected between 5° and 40° (2θ), with a step size of 0.0205° and a scan time lasting ca. 15 min. The diffraction patterns were calculated using Mercury6 with a step size of 0.2 and an FWHM of 0.1.

2.4. Topological Analysis

A topological analysis was performed with the TopCryst.com standard representation algorithm and represented with ToposPro [33–39]. The topology was calculated for $Zn_2(trz_2An)(trz)_2$ with or without the triazolyl substituent of the anilate linker.

The voids volume was calculated and represented using the contact surface method *via* the Mercury software (probe radius = 1.20 Å and grid spacing = 0.3 Å) [40]. The pore analysis was performed with the following parameters (temperature = 298 K; He probe σ = 2.58 Å; N_2 probe σ = 3.314 Å; He probe ε = 10.22 K; cutoff distance = 12.8 Å; cubelet size = 0.05 Å; number of samples per atom = 500). The calculated pore parameters are summarized in Table S2.

2.5. Spectroscopic Measurements

Raman spectra were obtained under ambient conditions on freshly prepared single crystals and microcrystalline powders with a micro-Raman spectrometer (Horiba XploRA PLUS) equipped with a solid-state laser (λ_{ex}: 785 nm) in the 500–2000 cm^{-1} spectral range, with a 50 LWD objective. A 180° reflective geometry was adopted. Samples were deposited on microscope glass slides, and the scattering peaks were calibrated against a Si standard (ν: 520.7 cm^{-1}). A typical spectrum was collected with a 15 s acquisition time and was averaged over 15 scans. No sample decomposition was observed during the experiments.

Infrared spectra of the powder samples were acquired in attenuated total reflectance (ATR) mode using a Bruker Equinox 55 spectrophotometer within the 400–4000 cm^{-1} spectral range for the complex and the ligands. Each spectrum was obtained by averaging

130 scans at a resolution of 4 cm^{-1}. Background spectra were measured under ambient conditions using a clean ATR crystal before each sample analysis.

2.6. Thermogravimetric Analysis (TGA)

TGA was performed in alumina crucibles with the Simultaneous Thermal Analyzer (STA) 6000 under nitrogen flux (40 mL/min) in the temperature range of 25–800 °C with a ramp of 10 °C/min.

2.7. Optical and Luminescence Properties

UV–Vis absorption spectra were recorded from 220 nm with an Agilent Technologies Cary 5000 UV-Vis-NIR Spectrophotometer. Solid-state samples placed between quartz slides were analyzed in terms of both total frontal transmittance modes (at the entrance of the integrating sphere) and total reflectance (on the back of the integrating sphere). Aqueous solutions of anilate salts (10^{-4} M) and well-mixed aqueous dispersions of the CP (0.5 g L^{-1}) were prepared and measured in 1.0 cm quartz cuvettes.

Emission spectra at fixed excitation wavelengths of the samples dispersed in solution or in solid state were collected using a Horiba-Jobin Yvon Fluoromax-3 spectrofluorometer equipped with a direct current Xenon lamp as the excitation source in a range of 320 to 550 nm, with a 2 nm slit for both excitation and emission and an integration time of 0.7 s. The three-dimensional fluorescence mapping (excitation–intensity–emission) of the samples dispersed in water under continuous stirring was performed with an excitation range of 280–500 nm and an emission range of 288–800 nm, with a 10 nm slit for excitation and emission and an integration time of 0.1 s; maps of the solid samples were collected with an excitation range of 280–500 nm and an emission range of 293–800 nm, with a 10 nm slit for excitation and 5 nm for emission and an integration time of 0.1 s.

3. Results

3.1. Crystal Structure

The SCXRD analysis revealed that the heteroleptic CP crystallizes in the monoclinic P21/c space group, with one zinc ion, one triazole linker, and half a trz_2An^{2-} linker in the asymmetric unit (Figure 2a, Table S1). No residual solvents were detected by SCXRD analysis or TGA (Figure S2), and no additional phases were observed by PXRD (Figure S3). The formula unit of the compound is therefore assigned as $Zn_2(trz_2An)(trz)_2$. The Zn^{II} ions are hexacoordinated with a distorted octahedral geometry (Figure 2b). The coordination sphere is composed of two oxygen atoms from the anilate (O1 and O2) with the typical cis bidentate coordination mode, one nitrogen atom from the triazolyl substituent (N3), and the three nitrogen atoms of the triazole linker (N4, N5, and N6) (Figure 2b).

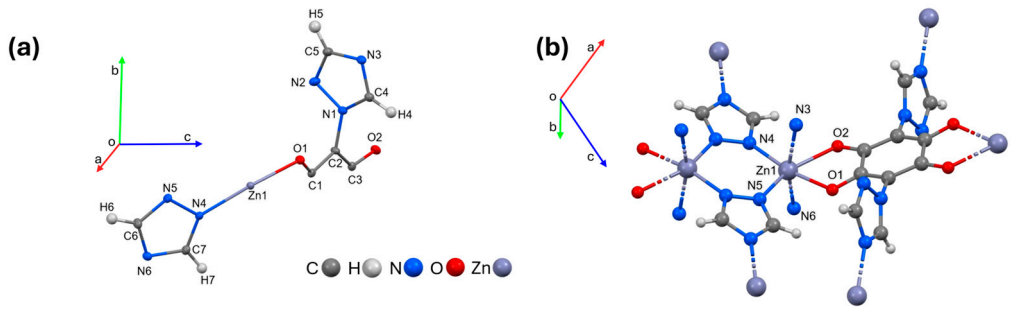

Figure 2. (**a**) The asymmetric unit of $Zn_2(trz_2An)(trz)_2$ (ellipsoid representation with 50% probability). (**b**) The coordination environment around the Zn^{II} nodes.

Interestingly, the crystal packing (Figure 3a) reveals a framework topology that resembles the one of CALF-20 and other similar compounds synthesized using different carboxylic acids [41–43]. Indeed, the Zn dimers, bridged by N4 and N5 (Figure 2b), are interconnected through N6, creating the typical 2D Zn-triazole layer (Figure 3b). The Zn-triazole layers are pillared by the anilate linker, resulting in an overall 3D connectivity. The triazolyl substituents further pillar the layers by coordinating adjacent Zn^{II} dimers via N3 (Figure 3c).

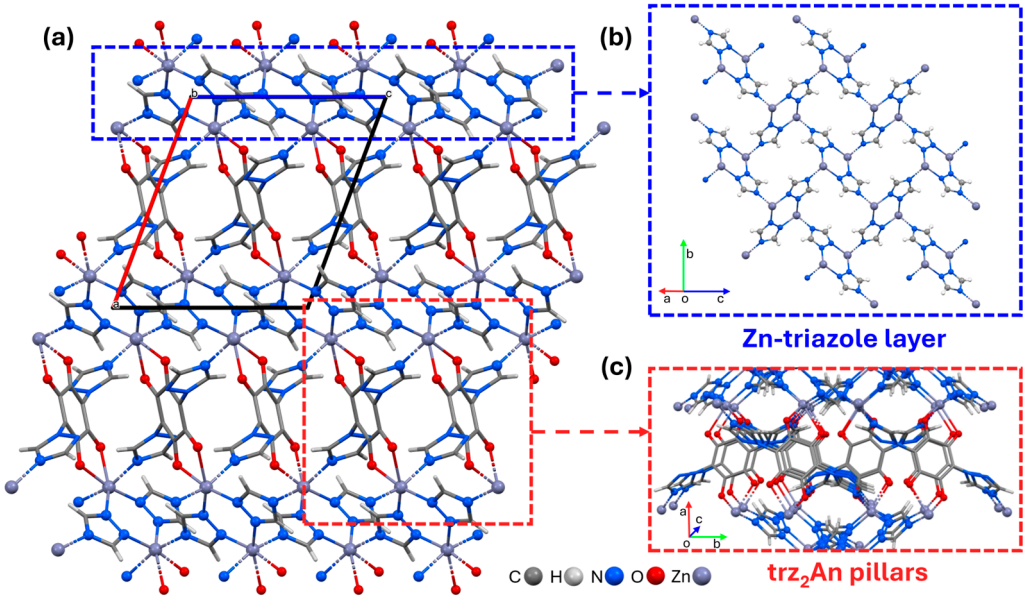

Figure 3. (**a**) Crystalline packing of $Zn_2(trz_2An)(trz)_2$ along the crystallographic *b* direction; (**b**) a single two-dimensional layer of Zn-triazole that extends along the *bc* plane; (**c**) representation along the *c* axis of the trz_2An^{2-} linkers, which act as pillars between the different Zn-triazole layers.

The Zn^{II} exhibits a larger coordination sphere (CN: 6) than CALF-20 (CN: 5) [15], along with slightly longer Zn-N distances (Table 1). In our case, the coordination mode results are comparable to that of the polymorph γ-CALF-20, where an additional coordinated water molecule can occupy this coordination position on half of the Zn^{II} [44]. Similarly to CALF-20 and its polymorphs [15,44], the Zn-O2 distance is longer and the Zn-O1 distance is much shorter and comparable to the Zn-N distances (Table 1). In general, the coordination of the two oxygen atoms is highly distorted in our case, although the pattern of distances obtained is comparable to that of γ-CALF-20. This can also be observed in other heteroleptic compounds containing anilate ligands, Zn^{II}, and nitrogen-containing co-ligands such as pyridine (CCDC number: 1546444) [45] and imidazole (CCDC number: 1568064) [46]. In these cases, the C–O distances differ (Table S2), suggesting less charge delocalization, mostly due to the purely electrostatic interaction between the oxygen atoms and the closed-shell and hard Zn^{II} ion. Consequently, one of the two oxygen atoms is more negatively charged and more strongly bonded. This is consistent with photophysical measurements showing properties that are largely comparable to those of the free ligand (which is also less delocalized). In general, the strong distortion of the coordination sphere can be attributed to this electronic/electrostatic effect, combined with the steric hindrance induced by the topology and closed-shell nature of Zn^{II}, which generally leads to less preferential directionality of the coordination bonds.

Table 1. Comparison between the coordination bond distances (Å) in $Zn_2(trz_2An)(trz)_2$, CALF-20 (CCDC numbers: 2084733) and γ-CALF-20 (CCDC numbers: 2265299).

$Zn_2(trz_2An)(trz)_2$		**CALF-20**		**γ-CALF-20**	
$Zn\text{-}O_{trz2An}$		$Zn\text{-}O_{ox}$		$Zn\text{-}O_{ox}$	
Zn-O1	2.088(1)	Zn-O1	2.022(2)	Zn-O1	2.082(4)
Zn-O2	2.383(1)	Zn-O2	2.189(3)	Zn-O2	2.198(3)
$Zn\text{-}N_{trz}$		$Zn\text{-}N_{trz}$		$Zn\text{-}N_{trz}$	
Zn-N4	2.070(2)	Zn-N1	2.007(2)	Zn-N1	2.079(4)
Zn-N5	2.099(2)	Zn-N2	2.091(3)	Zn-N3	2.028(5)
Zn-N6	2.104(2)	Zn-N3	2.016(3)	Zn-N4	2.082(4)
$Zn\text{-}N_{trz}$				$Zn\text{-}O_{w}$	
Zn-N3	2.192(2)			Zn-O3	2.319(7)

Contrary to CALF-20 and most of its analogues, $Zn_2(trz_2An)(trz)_2$ exhibits very limited accessibility to crystallization solvent and other guest molecules. In fact, the triazolyl substituent is located within the channels that run along the [101] plane through the tetrameric triazole rings, a common feature of these pillared structures (Figure 3 and Figure S4), creating significant steric hindrance. Consistently, the voids analysis reveals isolated cavities that account for only 3.3% of the cell volume (Figure S5). Furthermore, the pore analysis performed with Mercury shows that the LCD is 2.50 Å and the PLD is 1.77 Å, together with negligible network-accessible surface area and volume (Table S2). These observations imply that molecular access to and diffusion within the internal cavity of the framework are significantly restricted. Consequently, the compound is more appropriately classified as a 3D CP rather than an MOF. Indeed, according to the IUPAC definition [47], an MOF is nothing more than a multidimensional CP containing potential voids. These potential voids are merely a volume within the structure that can accommodate guest molecules of a reasonable size (1.2 Å in diameter can be used as the standard probe) [40,48]. In this regard, the effects of flexibility and structural variations induced by the guest are not considered [49], although in our case the structure is very compact and according to crystallography it contains no voids accessible to guest molecules. This dense packing along the pillars, together with the presence of the additional connectivity introduced by the triazole substituent, suggests that the structure has a small degree of flexibility and strong steric hindrance between the cavities. Indeed, although the typical rectangular voids described in the Zn-triazole layer are present (Figures 3, S3 and S4), they seem to be difficult to access even for a probe as small as water.

This interpretation is further supported by the TGA profile, which shows a negligible mass loss below 400 °C and a sharp decomposition event around 450 °C, consistent with the breakdown of the coordination polymer (Figure S2). Accordingly, we hypothesize that the interactions with water molecules are related to solvent polarity effects and/or changes in molecular rigidity (*vide infra*) rather than guest-mediated structural variation, contrary to what occurs in CALF-20 [44].

The high thermal stability is consistent with MOFs based on trz_2An^{2-} linkers and heteroleptic triazole-based 3D pillared MOFs [25,26,50]. The topology of $Zn_2(trz_2An)(trz)_2$, rationalized via the standard simplification algorithm using TopCryst (ST1-2; Figure S5), shows a 3D framework consisting of 2D layers composed of Zn^{II} and trz^- linkers that act as 3-c nodes, analogous to the Zn-triazole layer of CALF-20, pillared by trz_2An^{2-} linkers (Figure S4). In this system, the ancillary triazolyl substituent enables the anilate ligand to act as a 4-c node, while Zn^{II} becomes 5-connected, giving rise to a **3,4,5T35** topology distinct

from the **dmc** framework of CALF-20. In fact, the trz_2An features a pendant arm that further connects the Zn-triazole layers, acting as an additional pillar. From a topological perspective, this cannot be considered an edge (2-c node) but rather as a 4-c rectangular node. On the other hand, both structures exhibit a practically superimposable Zn-triazole layer (Figure S4) and a pillared structure, with the anilate moiety acting as a bidentate bridge in a manner analogous to that of the oxalate in CALF-20. As mentioned above, this additional connectivity may explain the high thermal stability (more typical of dense CP) and the reduced flexibility, induced by steric hindrance and Zn^{II} additional coordination, that prevents the incorporation of small guest molecules such as water (Figure S5).

To further verify the topological analogy with CALF-20-like materials, we recalculated the underlying topology, excluding the contribution of the triazolyl substituent (ST2; Figure S4). Under this simplification, the framework adopts a **dmc** topology analogous to that of CALF-20, confirming the close correspondence between the two structures (Figure S4). To the best of our knowledge, this represents the first incorporation of an anilate-type ligand into a CALF-20-like heteroleptic 3D pillared architecture; previous studies have mainly focused on replacing the oxalate ligand with alternative carboxylate-based linkers [27,28].

3.2. Coordination Environment Analysis

The degree of coordination between the building units within the framework was assessed by vibrational spectroscopy, monitoring changes in functional groups and molecular structure after the synthesis. Figure 4a compares the Raman spectrum under ambient conditions of free Htrz and H_2trz_2An linkers with that of the coordinated framework $Zn_2(trz_2An)(trz)_2$. The free anilate ligand exhibits the characteristic vibrational features of 2,5-dihydroxybenzoquinones (dhbq and H_2H_2An), with bands in the 1600–1660 cm^{-1} region corresponding to ν(C=C) and ν(C=O) stretching modes, and bands in the 750–890 cm^{-1} region mainly associated with O-H torsional (τ) vibrations [51].

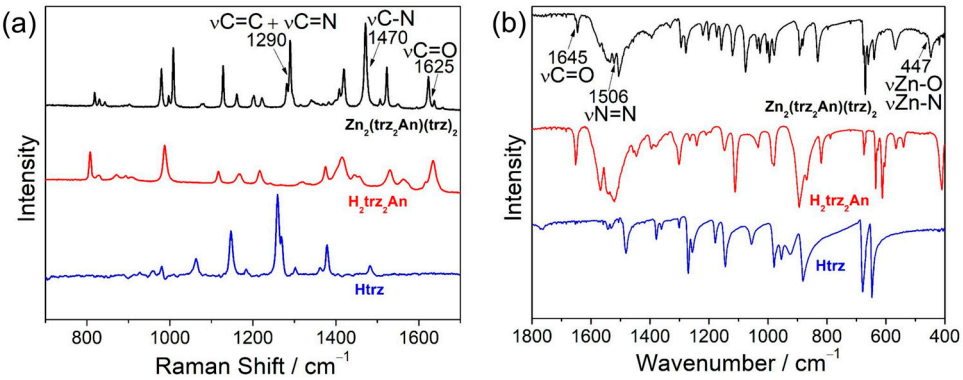

Figure 4. (**a**) Normalized Raman and (**b**) ATR FT-IR spectra of H_2trz_2An (red), Htrz (blue), and $Zn_2(trz_2An)(trz)_2$ (black).

While clearly present in the free ligands, these spectral features progressively shift or decrease in intensity upon coordination to the metal centers and concomitant formation of the polymeric framework. In particular, the shift of the anilate-based band from 1633 cm^{-1} in the free linker to 1625 cm^{-1} in the coordinated species, together with its increased intensity, indicates a weakening of the double-bond character of the terminal groups induced by metal binding. Additionally, the CP spectrum displays bands in the 1300–900 cm^{-1} region attributable to the N-heterocycle vibrations, supporting the integration of these linkers within the extended framework.

Consistent with the Raman analysis, the ATR FT-IR spectra (Figure 4b) likewise exhibit features characteristic of successful coordination of the building units and formation of

a phase-pure CP. The band centered at 1650 cm^{-1} and commonly assigned to ν(C=O) vibrational modes in free anilate linkers shifts to lower wavenumbers and decreases in intensity as the double-bond character of these functional groups weakens when coordinating metal ions in $Zn_2(trz_2An)(trz)_2$. Within the 1600–1450 cm^{-1} region, the Zn-based framework displays a broad absorption band attributable to overlapping ν(C=C) and ν(C=O) stretching modes, further confirming the presence of the benzoquinone cores. A distinct feature at approximately 1520 cm^{-1}, assigned to ν(N=N) vibration [52], appears downshifted relative to the free ligand, indicating effective coordination of the triazole moieties and redistribution of electron density upon coordination. The spectral features observed between 1400 and 920 cm^{-1} arise from triazolyl ring vibrations together with C–N stretching modes [52,53], confirming the presence of the heterocyclic linkers within the structure. Finally, the bands detected in the 470–420 cm^{-1} region correspond to M–N and M–O stretching vibrations, substantiating the coordination of the organic ligands to the metal centers [54].

3.3. Photophysical Properties

The photophysical investigation initiated with the examination of the uncoordinated linkers, thereby establishing the spectral signatures of the molecular building blocks. Thus, it was extended to the coordinated framework (Figure S6) to assess the effects of metal coordination and framework formation on its electronic structure. Spectroscopic measurements were performed above 220 nm in total reflectance (Figure 5a) and total frontal transmission modes (Figure S7) for both the crystalline linkers and the framework and by absorption spectroscopy for an aqueous solution of the anilate ligand and an aqueous dispersion of the polymer (Figure 5b).

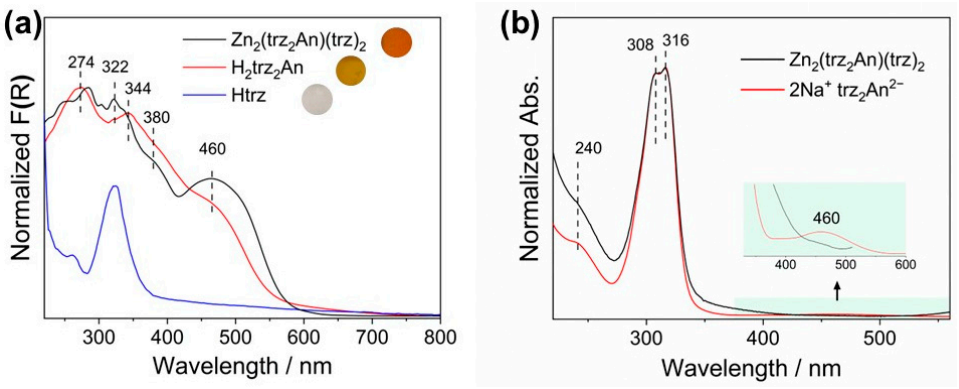

Figure 5. (**a**) UV-Vis total reflectance spectra of uncoordinated linkers H_2trz_2An and Htrz and the coordination framework $Zn_2(trz_2An)(trz)_2$ measured as dry powders (inset: optical pictures of the powder samples). (**b**) Absorption spectra of an aqueous salt solution of the uncoordinated ligand $2Na^+trz_2An^{2-}$ and an aqueous dispersion of $Zn_2(trz_2An)(trz)_2$.

The Htrz linker is a weakly photosensitive species and appears as a crystalline white powder in the solid state, showing well-defined absorption bands exclusively below 390 nm, with λ_{max} at approximately 260 and 325 nm. The higher-energy band is assigned to intraligand $\pi \rightarrow \pi^*$ transitions. In contrast, the lower-energy feature is attributed to scattering effects associated with the measurement in total reflectance mode rather than to a genuine electronic transition (Figure 5a). The interpretation is supported by the complete disappearance of the band at 325 nm when the same sample was measured in total frontal transmittance mode (Figure S7). Furthermore, isolated Htrz molecules are reported to exhibit electronic transitions 260 nm [55]. The absence of significant absorption above 400 nm indicates that Htrz contributes only marginally to the photosensitization mechanisms of the framework compared to the anilate linkers.

The H_2trz_2An linker is a stronger photosensitive species and appears as a light-brown crystalline powder in the solid state. In total reflectance mode, it displays a broad absorption profile comprising multiple bands and shoulders (Figure 5a) indicative of a complex manifold of molecular and intermolecular electronic transitions. Consistent with our analysis of non-functionalized dhbq and with the corresponding total frontal transmittance measurements (Figures S7 and S7a), the dominant absorption features are located in the UV region [56–58]. The spectrum is characterized by a broad band centered at approximately 320 nm, together with shoulders around 380 nm and 460 nm. Interestingly, although triazolyl functionalization significantly affects the position and intensity of these features, it does not give rise to any distinct additional absorption band that can be unambiguously attributed to the triazolyl substituent compared to the dhbq. To further disentangle the effects of crystal packing and intermolecular interactions from the intensity electronic properties of the anilate, the absorption spectrum of H_2trz_2An was subsequently investigated in basic aqueous medium. This resulted in a better-resolved absorption profile and a redistribution of the relative intensities of the individual absorption bands (Figure 5b). The main bands below 400 nm become sharper, in agreement with the behavior of dhbq and further confirming the anilate electronic core (Figure S9). At the same time, triazolyl functionalization induces a more pronounced blue-shift compared to dhbq, reflecting the effective modulation of the linker electronic structure. In contrast, the broad absorption feature above 400 nm remains centered around 460 nm and spans a similar spectral range, although with a visibly reduced intensity compared to the solid sample. This behavior is consistent with the intrinsic tendency of anilates to absorb predominantly in the UV region rather than in the visible range. Consequently, the periodic arrangement of H_2trz_2An within the polymer framework is expected to give rise primarily to UV absorption features, with only a minor contribution to the visible spectral region.

With the electronic transitions of the isolated linkers established, attention was then directed to the coordination framework to evaluate how metal coordination and periodic organization influence its photophysical properties. Just as expected, dry orange crystals of $Zn_2(trz_2An)(trz)_2$ (Figure S6) are characterized by a strong and complex absorption above 220 nm with multiple absorption bands and shoulders in spectral regions comparable to those of the uncoordinated anilate moiety (Figures 5a and S7). Across the 300–750 nm range, the spectra recorded in total reflectance and total frontal transmittance mode are essentially superimposable, indicating that scattering contributions and intermolecular effects do not significantly alter the intrinsic absorption profile of the crystalline material (Figure S8b).

The coordination framework exhibits absorption edge shifts and changes in relative band intensities compared to the free H_2trz_2An linkers, consistent with reduced intermolecular interactions upon incorporation into the framework. In particular, the absorption feature above 400 nm becomes more pronounced in the framework, consistent with the observed color change from light brown (uncoordinated anilate linker) to orange (solid-state framework). Overall, the electronic structure is largely dominated by the anilate unit and its coordination with Zn clusters above 250 nm, while contributions from trz^- moieties remain limited.

For a direct assessment of the intrinsic electronic behavior of the anilates' photosensitivity, their photophysical response was additionally studied in an aqueous dispersion of the material and directly compared with that of the free linker dissolved in solution and the crystalline solid framework. Upon dispersion in water (Figure 5b), the polymeric framework retains a UV absorption profile overlapping with that of the uncoordinated linker, while the visible absorption band undergoes a blue-shift and a reduction in intensity. This behavior is consistent with solvent-mediated stabilization of radiative relaxation chan-

nels in the dispersed state, which allows a more ligand-centered photophysical response to emerge without any change in the integrity or electronic structure of the coordination framework. The presence of redox-inert Zn^{II} nodes further supports the predominance of ligand-centered excited states, as metal-based charge-transfer processes are not expected to significantly contribute to the relaxation pathways.

To further confirm the molecular nature of the excited states, PL spectroscopy was employed to investigate the photoinduced relaxation pathways of both the uncoordinated anilate linkers and the coordinated framework. In the solid state, no detectable emission was observed for either system under ambient conditions this implies that nonradiative relaxation channels (e.g., intermolecular self-quenching and vibrational channels) dominate for both uncoordinated and coordinated linkers despite strong absorption in the UV region (Figure 5). Upon dispersion in water, however, both systems exhibit measurable emission, which is consistent with a partial and solvent-modulated suppression of nonradiative relaxation channels.

In the case of the uncoordinated linker salt (Figure 6a,c), two excitation–emission features are identified, centered approximately at λ_{ex}: 340 nm–λ_{em}: 425 nm and λ_{ex}: 376 nm–λ_{em}: 495 nm, with comparable emission intensities. Notably, both the excitation maxima show limited overlap with the absorption profile, indicating that only a subset of the populated excited states contributes to emission (Figure 6c). These results suggest that the luminescence of the uncoordinated linker is recovered in aqueous medium, likely due to the suppression of intermolecular self-quenching and stabilization of charged excited states. However, the relatively modest emission contribution indicates that radiative relaxation remains a minor deactivation pathway, with nonradiative decay still dominating the excited-state dynamics. A similar dominance of nonradiative decay is also observed for the sodium salt solution of dhbq, which, however, displays only a single excitation-emission feature (λ_{ex}: 340 nm–λ_{em}: 424 nm; Figure S10) under similar conditions, highlighting the different electronic structure of the two linkers and the luminescent nature of the anilate moiety.

Meanwhile, the coordination framework dispersion exhibits a single dominant feature (λ_{ex}: 340 nm–λ_{em}: 425 nm), indicating the presence of one principal emissive state and a single radiative relaxation pathway (Figure 6b). The confinement of the excitation and emission profiles within this narrow spectral region implies a well-defined electronic transition (Figure 6d). Furthermore, the similarity of these spectral ranges for the framework dispersion to those of the free anilate solution (Figure 6c,d) supports a predominantly linker-centered emission mechanism. However, it also indicates that, while luminescence is once again recovered in aqueous medium, coordination with Zn^{II} cations perturbs the electronic structure of the organic linker trz_2An^{2-}, selectively suppressing lower-energy emissive states (i.e., λ_{ex}: 376 nm–λ_{em}: 495 nm). These findings underscore that, similarly to other frameworks previously reported [59–62], our coordination framework may act as a bulk insulator under ambient conditions, with strongly localized charge carriers and limited dielectric screening. On the other hand, interactions with polar molecules such as H_2O may lead to a locally polarized environment within the framework responsible for stabilizing photoinduced excited states and promoting radiative relaxation pathways [63–65]. Overall, these results highlight the role of coordination and intermolecular interactions in modulating the balance between radiative and nonradiative relaxation processes.

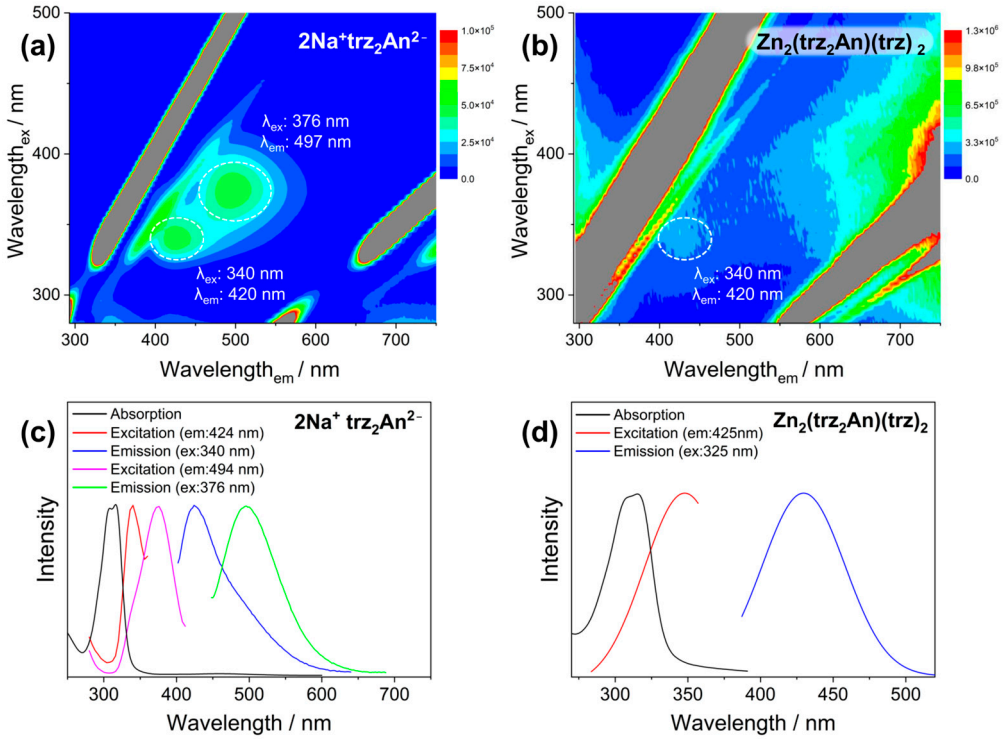

Figure 6. 2D PL maps (wavelength excitation (y)–wavelength emission (x)–intensity (false color scale) of (**a**) the uncoordinated linker $2Na^{+}trz_2An^{2-}$ aqueous solution (0.027 g L^{-1}) and (**b**) the coordination polymer $Zn_2(trz_2An)(trz)_2$ aqueous dispersion (0.5 g L^{-1}) under stirring with highlighted luminescent features (dashed lines). Steady-state UV-Vis absorption (black line) and PL spectroscopic characterizations (excitation: red and pink lines; emission: blue and green lines) of (**c**) an aqueous solution of the $2Na^{+}trz_2An^{2-}$ linker and (**d**) an aqueous dispersion of $Zn_2(trz_2An)(trz)_2$ (0.5 g L^{-1}).

4. Conclusions

In conclusion, this work demonstrates that the introduction of π-conjugated triazolyl-functionalized anilate linkers into CALF-20-type architectures does not simply yield isoreticular analogues but instead drives the formation of structurally related yet electronically distinct frameworks. The resulting material combines the structural robustness of CALF-20 with ligand-centered luminescence, underscoring how subtle modifications in linker electronics can profoundly alter the photophysical response of coordination polymers. This highlights heteroleptic design as a powerful approach for accessing multifunctional, light-responsive frameworks beyond conventional CALF-20 chemistry.

Supplementary Materials: The following supporting information can be downloaded at https://www.mdpi.com/article/10.3390/cryst16070445/s1, Figure S1: Raman spectra of (a) samples synthesized in different batches and (b) immersed in water for several hours; Figure S2: TGA profile of the sample under a nitrogen atmosphere; Figure S3: PXRD pattern calculated from the CIF structure compared with the experimental powder diffraction pattern. Figure S4: Representation of the topology obtained with ToposPro for a) $Zn_2(trz_2An)(trz)_2$ and b) for the same CP omitting the triazolyl substituents from the anilate *core*. A comparison between the crystal packing of (c) $Zn_2(trz_2An)(trz)_2$ and (d) CALF-20 (CCDC number: 2084733) along the *b* direction; Figure S5: Representation of the isolated cavities localized within $Zn_2(trz_2An)(trz)_2$; Figure S6: Microscopy image of the heteroleptic Zn^{II} coordination polymer collected using microRaman instrumentation; Figure S7: UV-Vis spectra of powder samples measured in total frontal transmission mode; Figure S8: Comparison of UV-Vis spectra of powder samples measured in total reflectance and total frontal transmission mode; Figure S9: Comparison of normalized UV-Vis absorption spectra of aqueous $2Na^{+}$ trz_2An^{2-} and $2Na^{+}$ H_2An^{2-} solutions (10^{-4} M); Figure S10: (a) 2D map (excitation (y)–emission

(x)–intensity (false color scale)) and (b) comparison between steady-state UV-Vis absorption and PL spectroscopic profiles of an aqueous solution of $2Na^{+}H_2An^{2-}$ (10^{-4} M); Table S1: Crystal data and structure refinement for $Zn_2(trz_2An)(trz)_2$; Table S2: The pore analysis results for $Zn_2(trz_2An)(trz)_2$; Table S3: The Pore Analysis results for $Zn_2(trz_2An)(trz)_2$.

Author Contributions: Conceptualization, F.M. and M.L.M.; methodology, F.M., P.R., E.C. and M.O.; data curation, F.M., P.R., E.C. and M.O.; original draft preparation, F.M., P.R., E.C. and M.O.; writing—review and editing, F.M., P.R., E.C., M.O., L.M. and M.L.M.; crystallography, F.M.; optical characterization, P.R.; supervision, F.M. and M.L.M.; funding acquisition, M.L.M. All authors have read and agreed to the published version of the manuscript.

Funding: This research was funded by the Fondazione di Sardegna e gli Atenei Sardi, Regione Sardegna, (i) L.R. 7/2007 annualità 2022, project VOC_3D, "3D printed optical VOC sensors for indoor air quality evaluation", CUP F73C23001590007, (ii) L.R. 7/2007 annualità 2023, Project "Advances in porous sorbents and catalysts for synthetic natural gas production by H2S removal and COx methanation" CUP F23C25000170007.

Data Availability Statement: The data presented in this study are available on request from the corresponding author.

Acknowledgments: The CeSAR (Centro Servizi d'Ateneo per la Ricerca) is acknowledged for X-Ray diffraction measurements. We thank bando Vinci2025 for the E.C. PhD grant. During the preparation of this manuscript, the authors used DeepL and ChatGPT (GPT-5.5) for the purposes of English and grammar editing. The authors have reviewed and edited the output and take full responsibility for the content of this publication.

Conflicts of Interest: The authors declare no conflicts of interest.

References

1. Eddaoudi, M.; Kim, J.; Rosi, N.; Vodak, D.; Wachter, J.; O'Keeffe, M.; Yaghi, O.M. Systematic design of pore size and functionality in isoreticular MOFs and their application in methane storage. *Science* **2002**, *295*, 469–472. [CrossRef] [PubMed]
2. Furukawa, H.; Gándara, F.; Zhang, Y.B.; Jiang, J.; Queen, W.L.; Hudson, M.R.; Yaghi, O.M. Water adsorption in porous metal-organic frameworks and related materials. *J. Am. Chem. Soc.* **2014**, *136*, 4369–4381. [CrossRef] [PubMed]
3. Yaghi, O.M.; Kalmutzki, M.J.; Diercks, C.S. *Introduction to Reticular Chemistry: Metal-Organic Frameworks and Covalent Organic Frameworks*; Wiley-VCH Verlag GmbH & Co. KGaA: Weinheim, Germany, 2019; p. 509.
4. Li, F.-L.; Wang, P.; Huang, X.; Young, D.J.; Wang, H.-F.; Braunstein, P.; Lang, J.-P. Large-Scale, Bottom-Up Synthesis of Binary Metal–Organic Framework Nanosheets for Efficient Water Oxidation. *Angew. Chem. Int. Ed.* **2019**, *58*, 7051–7056. [CrossRef] [PubMed]
5. Ashoka Sahadevan, S.; Monni, N.; Oggianu, M.; Abhervé, A.; Marongiu, D.; Saba, M.; Mura, A.; Bongiovanni, G.; Mameli, V.; Cannas, C.; et al. Heteroleptic NIR-Emitting Yb^{III}/Anilate-Based Neutral Coordination Polymer Nanosheets for Solvent Sensing. *ACS Appl. Nano Mater.* **2020**, *3*, 94–104. [CrossRef]
6. Zhang, J.; Li, P.; Zhang, X.; Ma, X.; Wang, B. Aluminum Metal-Organic Frameworks with Photocatalytic Antibacterial Activity for Autonomous Indoor Humidity Control. *ACS Appl. Mater. Interfaces* **2020**, *12*, 46057–46064. [CrossRef] [PubMed]
7. Du, C.; Zhang, Z.; Yu, G.; Wu, H.; Chen, H.; Zhou, L.; Zhang, Y.; Su, Y.; Tan, S.; Yang, L.; et al. A review of metal organic framework (MOFs)-based materials for antibiotics removal via adsorption and photocatalysis. *Chemosphere* **2021**, *272*, 129501. [CrossRef] [PubMed]
8. Monni, N.; Baldoví, J.J.; García-López, V.; Oggianu, M.; Cadoni, E.; Quochi, F.; Clemente-León, M.; Mercuri, M.L.; Coronado, E. Reversible tuning of luminescence and magnetism in a structurally flexible erbium–anilato MOF. *Chem. Sci.* **2022**, *13*, 7419–7428. [CrossRef] [PubMed]
9. Rassu, P.; Ma, X.; Wang, B. Engineering of catalytically active sites in photoactive metal–organic frameworks. *Coord. Chem. Rev.* **2022**, *465*, 214561. [CrossRef]
10. Cametti, M. 1D coordination polymers as promising adsorbers for volatile organic pollutants: The case of bispidine based materials. *Coord. Chem. Rev.* **2026**, *549*, 217261. [CrossRef]
11. Furukawa, H.; Müller, U.; Yaghi, O.M. "Heterogeneity within Order" in Metal–Organic Frameworks. *Angew. Chem. Int. Ed.* **2015**, *54*, 3417–3430. [CrossRef] [PubMed]
12. Pullen, S.; Clever, G.H. Mixed-Ligand Metal–Organic Frameworks and Heteroleptic Coordination Cages as Multifunctional Scaffolds—A Comparison. *Acc. Chem. Res.* **2018**, *51*, 3052–3064. [CrossRef] [PubMed]

13. Daolio, A.; Giovanardi, D.; Mazzeo, P.P.; Pelagatti, P.; Bacchi, A. The dynamic adaptability of mixed-ligand zinc MOFs: From fundaments to applications. *Coord. Chem. Rev.* **2026**, *553*, 217509. [CrossRef]
14. Ashoka Sahadevan, S.; Manna, F.; Abhervé, A.; Oggianu, M.; Monni, N.; Mameli, V.; Marongiu, D.; Quochi, F.; Gendron, F.; Le Guennic, B.; et al. Combined Experimental/Theoretical Study on the Luminescent Properties of Homoleptic/Heteroleptic Erbium(III) Anilate-Based 2D Coordination Polymers. *Inorg. Chem.* **2021**, *60*, 17765–17774. [CrossRef] [PubMed]
15. Lin, J.-B.; Nguyen, T.T.T.; Vaidhyanathan, R.; Burner, J.; Taylor, J.M.; Durekova, H.; Akhtar, F.; Mah, R.K.; Ghaffari-Nik, O.; Marx, S.; et al. A scalable metal-organic framework as a durable physisorbent for carbon dioxide capture. *Science* **2021**, *374*, 1464–1469. [CrossRef] [PubMed]
16. Chen, Z.; Ho, C.-H.; Wang, X.; Vornholt, S.M.; Rayder, T.M.; Islamoglu, T.; Farha, O.K.; Paesani, F.; Chapman, K.W. Humidity-Responsive Polymorphism in CALF-20: A Resilient MOF Physisorbent for CO_2 Capture. *ACS Mater. Lett.* **2023**, *5*, 2942–2947. [CrossRef]
17. Magnin, Y.; Dirand, E.; Maurin, G.; Llewellyn, P.L. Abnormal CO_2 and H2O Diffusion in CALF-20(Zn) Metal–Organic Framework: Fundamental Understanding of CO_2 Capture. *ACS Appl. Nano Mater.* **2023**, *6*, 19963–19971. [CrossRef]
18. Oktavian, R.; Goeminne, R.; Glasby, L.T.; Song, P.; Huynh, R.; Qazvini, O.T.; Ghaffari-Nik, O.; Masoumifard, N.; Cordiner, J.L.; Hovington, P.; et al. Gas adsorption and framework flexibility of CALF-20 explored via experiments and simulations. *Nat. Commun.* **2024**, *15*, 3898. [CrossRef] [PubMed]
19. Fan, D.; Naskar, S.; Maurin, G. Unconventional mechanical and thermal behaviours of MOF CALF-20. *Nat. Commun.* **2024**, *15*, 3251. [CrossRef] [PubMed]
20. Kang, D.A.; Suphavilai, N.; Mohamed, A.M.O.; Economou, I.G.; Shetty, M.; Kim, J.; Jeong, H.-K. Thermally-induced phase transformations of CALF-20: Insights into its phase stability and carbon capture properties. *J. Mater. Chem. A* **2025**, *13*, 18892–18899. [CrossRef]
21. Drwęska, J.; Roztocki, K.; Janiak, A.M. Advances in chemistry of CALF-20, a metal–organic framework for industrial gas applications. *Chem. Commun.* **2025**, *61*, 1032–1047. [CrossRef] [PubMed]
22. Attallah, A.G.; Bon, V.; Hirschmann, E.; Butterling, M.; Wagner, A.; Zaleski, R.; Kaskel, S. Uncovering the Dynamic CO_2 Gas Uptake Behavior of CALF-20 (Zn) under Varying Conditions via Positronium Lifetime Analysis. *Small* **2025**, *21*, 2500544. [CrossRef] [PubMed]
23. Monni, N.; Angotzi, M.S.; Oggianu, M.; Sahadevan, S.A.; Mercuri, M.L. Redox-active benzoquinones as challenging "non-innocent" linkers to construct 2D frameworks and nanostructures with tunable physical properties. *J. Mater. Chem. C* **2022**, *10*, 1548–1572. [CrossRef]
24. Monni, N.; Dey, S.; García-López, V.; Oggianu, M.; Baldoví, J.J.; Mercuri, M.L.; Clemente-León, M.; Coronado, E. Tunable SIM properties in a family of 3D anilato-based lanthanide-MOFs. *Inorg. Chem. Front.* **2024**, *11*, 5913–5923. [CrossRef] [PubMed]
25. Oggianu, M.; Manna, F.; Mameli, V.; Cannas, C.; Guiotto, V.; Crocellà, V.; Quesada, S.; Sassone, D.; Sacco, A.; Gallo Stampino, I.I.; et al. A 3D polymorphic Cu-based ultramicroporous MOF capable of CO_2 Uptake and Conversion. *J. Mater. Chem. A* **2026**, *14*, 9301–9315. [CrossRef]
26. Manna, F.; Monni, N.; Oggianu, M.; Clemente-Juan, J.M.; Clemente-León, M.; Mercuri, M.L. Thermally Stable Anilate-Based 3D CPs/MOFs. *Crystals* **2025**, *15*, 570. [CrossRef]
27. Gopalsamy, K.; Fan, D.; Naskar, S.; Magnin, Y.; Maurin, G. Engineering of an Isoreticular Series of CALF-20 Metal–Organic Frameworks for CO_2 Capture. *ACS Appl. Eng. Mater.* **2024**, *2*, 96–103. [CrossRef]
28. Croce, F.D.; Bresciani, G.; Taddei, M. Squarate-base isoreticular analogue of CALF-20: Fact or fiction? *ChemRxiv* **2026**, *2026*. [CrossRef] [PubMed]
29. Gauβ, W.; Heitzer, H.; Petersen, S. Umsetzungen von Chinonen mit stickstoffhaltigen Heteroaromaten. *Justus Liebigs Ann. Chem.* **1973**, *764*, 131–144. [CrossRef]
30. Dolomanov, O.V.; Bourhis, L.J.; Gildea, R.J.; Howard, J.A.K.; Puschmann, H. OLEX2: A complete structure solution, refinement and analysis program. *J. Appl. Cryst.* **2009**, *42*, 339–341. [CrossRef]
31. Sheldrick, G. SHELXT—Integrated space-group and crystal-structure determination. *Acta Cryst. A* **2015**, *71*, 3–8. [CrossRef] [PubMed]
32. Sheldrick, G. Crystal structure refinement with SHELXL. *Acta Cryst. C* **2015**, *71*, 3–8. [CrossRef] [PubMed]
33. Shevchenko, A.P.; Shabalin, A.A.; Karpukhin, I.Y.; Blatov, V.A. Topological representations of crystal structures: Generation, analysis and implementation in the TopCryst system. *STAM Methods* **2022**, *2*, 250–265. [CrossRef]
34. Blatov, V.A.; Shevchenko, A.P.; Proserpio, D.M. Applied Topological Analysis of Crystal Structures with the Program Package ToposPro. *Cryst. Growth Des.* **2014**, *14*, 3576–3586. [CrossRef]
35. O'Keeffe, M.; Peskov, M.A.; Ramsden, S.J.; Yaghi, O.M. The Reticular Chemistry Structure Resource (RCSR) Database of, and Symbols for, Crystal Nets. *Acc. Chem. Res.* **2008**, *41*, 1782–1789. [CrossRef] [PubMed]

36. Alexandrov, E.V.; Blatov, V.A.; Kochetkov, A.V.; Proserpio, D.M. Underlying nets in three-periodic coordination polymers: Topology, taxonomy and prediction from a computer-aided analysis of the Cambridge Structural Database. *CrystEngComm* **2011**, *13*, 3947–3958. [CrossRef]
37. Shevchenko, A.P.; Blatov, V.A. Simplify to understand: How to elucidate crystal structures? *Struct. Chem.* **2021**, *32*, 507–519. [CrossRef]
38. Alexandrov, E.V.; Shevchenko, A.P.; Blatov, V.A. Topological Databases: Why Do We Need Them for Design of Coordination Polymers? *Cryst. Growth Des.* **2019**, *19*, 2604–2614. [CrossRef]
39. Günther, M.; Blätte, D.; Oechsle, A.L.; Rivas, S.S.; Yousefi Amin, A.A.; Müller-Buschbaum, P.; Bein, T.; Ameri, T. Increasing Photostability of Inverted Nonfullerene Organic Solar Cells by Using Fullerene Derivative Additives. *ACS Appl. Mater. Interfaces* **2021**, *13*, 19072–19084. [CrossRef] [PubMed]
40. Macrae, C.F.; Sovago, I.; Cottrell, S.J.; Galek, P.T.A.; McCabe, P.; Pidcock, E.; Platings, M.; Shields, G.P.; Stevens, J.S.; Towler, M.; et al. Mercury 4.0: From visualization to analysis, design and prediction. *J. Appl. Cryst.* **2020**, *53*, 226–235. [CrossRef] [PubMed]
41. Ling, Y.; Chen, Z.; Zheng, H.; Zhou, Y.; Weng, L.; Zhao, D. Two Novel Zinc(II) Metal–Organic Frameworks Based on Triazole-Carboxylate Shared Paddle-Wheel Units: Synthesis, Structure, and Gas Adsorption. *Cryst. Growth Des.* **2011**, *11*, 2811–2816. [CrossRef]
42. Liu, J.; Wang, H.; Li, J. Pillar-layer Zn–triazolate–dicarboxylate frameworks with a customized pore structure for efficient ethylene purification from ethylene/ethane/acetylene ternary mixtures. *Chem. Sci.* **2023**, *14*, 5912–5917. [CrossRef] [PubMed]
43. Huang, X.; Ma, D.; Liu, X.-Y.; Qu, L.; Wang, B.; Feng, X. An ultramicroporous pillar-layered metal–organic framework for propylene/propane separation. *Chem. Commun.* **2025**, *61*, 19453–19456. [CrossRef] [PubMed]
44. Drwęska, J.; Formalik, F.; Roztocki, K.; Snurr, R.Q.; Barbour, L.J.; Janiak, A.M. Unveiling Temperature-Induced Structural Phase Transformations and CO_2 Binding Sites in CALF-20. *Inorg. Chem.* **2024**, *63*, 19277–19286. [CrossRef] [PubMed]
45. Nan, L.; Li-Fang, Z.; Yun, Z. Crystal structure of (3,6-dioxocyclohexa-1,4-diene-1,4-bis(olato)-κ^4O,O′:O″,O‴)-bis(tris(2-pyridylmethyl)amine-κ^4N,N′,N″,N‴))-dizinc(II) bis(hexafluorophosphate(V)), $C_{42}H_{38}F_{12}N_8O_4P_2Zn_2$. *Z. Kristallogr.—New Cryst. Struct.* **2017**, *232*, 657–659. [CrossRef]
46. Kingsbury, C.J.; Abrahams, B.F.; Robson, R. Crystal structure of catena-(bis(μ-2,5-dichloro-3,6-dioxycyclohexa-2,5-diene-1,4-dione)-bis(μ-1,1′-[1,4-phenylenebis(methylene)]bis(1H-imidazole))-di-zinc(ii) tetrahydrate). *CCDC* **2017**, 1568064. [CrossRef]
47. Batten, S.R.; Champness, N.R.; Chen, X.-M.; Garcia-Martinez, J.; Kitagawa, S.; Öhrström, L.; O'Keeffe, M.; Suh, M.P.; Reedijk, J. Terminology of metal–organic frameworks and coordination polymers (IUPAC Recommendations 2013). *Pure Appl. Chem.* **2013**, *85*, 1715–1724. [CrossRef]
48. Turner, M.J.; McKinnon, J.J.; Jayatilaka, D.; Spackman, M.A. Visualisation and characterisation of voids in crystalline materials. *CrystEngComm* **2011**, *13*, 1804–1813. [CrossRef]
49. Shimada, T.; Usov, P.M.; Wada, Y.; Ohtsu, H.; Watanabe, T.; Adachi, K.; Hashizume, D.; Matsumoto, T.; Kawano, M. Long Time CO_2 Storage Under Ambient Conditions in Isolated Voids of a Porous Coordination Network Facilitated by the "Magic Door" Mechanism. *Adv. Sci.* **2024**, *11*, 2307417. [CrossRef] [PubMed]
50. Monni, N.; Andres-Garcia, E.; Caamaño, K.; García-López, V.; Clemente-Juan, J.M.; Giménez-Marqués, M.; Oggianu, M.; Cadoni, E.; Mínguez Espallargas, G.; Clemente-León, M.; et al. A thermally/chemically robust and easily regenerable anilato-based ultramicroporous 3D MOF for CO_2 uptake and separation. *J. Mater. Chem. A* **2021**, *9*, 25189–25195. [CrossRef]
51. Pawlukojć, A.; Natkaniec, I.; Nowicka-Scheibe, J.; Grech, E.; Sobczyk, L. Inelastic neutron scattering (INS) studies on 2,5-dihydroxy-1,4-benzoquinone (DHBQ). *Spectrochim. Acta Part A Mol. Biomol. Spectrosc.* **2003**, *59*, 537–542. [CrossRef] [PubMed]
52. Billes, F.; Ziegler, I.; Mikosch, H. Vibrational spectroscopic study of sodium-1,2,4-triazole, an important intermediate compound in the synthesis of several active substances. *Spectrochim. Acta Part A Mol. Biomol. Spectrosc.* **2016**, *153*, 349–362. [CrossRef] [PubMed]
53. Krishnakumar, V.; Jayamani, N.; Mathammal, R. Molecular structure, vibrational spectral studies of pyrazole and 3,5-dimethyl pyrazole based on density functional calculations. *Spectrochim. Acta Part A Mol. Biomol. Spectrosc.* **2011**, *79*, 1959–1968. [CrossRef] [PubMed]
54. Xu, C.; Qiao, J.; Dong, S.; Zhou, Y.; Liu, X.; Feng, X. Asymmetric synthesis of dihydro-1,3-dioxepines by Rh(ii)/Sm(iii) relay catalytic three-component tandem [4 + 3]-cycloaddition. *Chem. Sci.* **2021**, *12*, 5458–5463. [CrossRef] [PubMed]
55. Palmer, M.H.; Camp, P.J.; Hoffmann, S.V.; Jones, N.C.; Head, A.R.; Lichtenberger, D.L. The electronic states of 1,2,4-triazoles: A study of 1H- and 1-methyl-1,2,4-triazole by vacuum ultraviolet photoabsorption and ultraviolet photoelectron spectroscopy and a comparison with ab initio configuration interaction computations. *J. Chem. Phys.* **2012**, *136*. [CrossRef] [PubMed]
56. Ahmed, M.; Khan, Z.H. Electronic absorption spectra of benzoquinone and its hydroxy substituents and effect of solvents on their spectra. *Spectrochim. Acta Part A Mol. Biomol. Spectrosc.* **2000**, *56*, 965–981. [CrossRef] [PubMed]
57. Sůra, R.; Antalík, M. Determination of proton dissociation constants (pKa) of hydroxyl groups of 2,5-dihydroxy-1,4-benzoquinone (DHBQ) by UV–Vis, fluorescence and ATR-FTIR spectroscopy. *Spectrochim. Acta Part A Mol. Biomol. Spectrosc.* **2022**, *271*, 120863. [CrossRef] [PubMed]

58. Manna, F.; Oggianu, M.; Galán-Mascarós, J.R.; Pop, F.; Le Guennic, B.; Mercuri, M.L.; Avarvari, N. Tuning the slow magnetic relaxation with the substituents in anilate bridged bis(dysprosium) complexes. *Dalton Trans.* **2024**, *53*, 8369–8381. [CrossRef] [PubMed]
59. Scatena, R.; Guntern, Y.T.; Macchi, P. Electron Density and Dielectric Properties of Highly Porous MOFs: Binding and Mobility of Guest Molecules in $Cu_3(BTC)_2$ and $Zn_3(BTC)_2$. *J. Am. Chem. Soc.* **2019**, *141*, 9382–9390. [CrossRef] [PubMed]
60. Chen, X.; Sapchenko, S.; Lu, W.; Li, M.; He, M.; Chen, Y.; Frogley, M.D.; da Silva, I.; Yang, S.; Schröder, M. Impact of Host–Guest Interactions on the Dielectric Properties of MFM-300 Materials. *Inorg. Chem.* **2023**, *62*, 17157–17162. [CrossRef] [PubMed]
61. Rassu, P.; Cappai, L.; Stagi, L.; Liu, R.; Enzo, S.; Mulas, G.; Garroni, S.; Malfatti, L.; Innocenzi, P.; Ma, X.; et al. Elucidating charge-transfer mechanisms and their effect on the light-induced reactivity of metastable MIL-125(Ti). *Appl. Catal. B* **2024**, *345*, 123692. [CrossRef]
62. Balendra; Kalita, R.; Ali, M.; Sanyukta; Murugavel, S.; Manna, K. A multifunctional manganese coordination polymer with polar solvent-responsive tunable dielectric properties and selective catalysis. *J. Mater. Chem. C* **2025**, *13*, 21122–21131. [CrossRef]
63. Allendorf, M.D.; Bauer, C.A.; Bhakta, R.K.; Houk, R.J.T. Luminescent metal–organic frameworks. *Chem. Soc. Rev.* **2009**, *38*, 1330–1352. [CrossRef] [PubMed]
64. Liu, J.-Q.; Luo, Z.-D.; Pan, Y.; Kumar Singh, A.; Trivedi, M.; Kumar, A. Recent developments in luminescent coordination polymers: Designing strategies, sensing application and theoretical evidences. *Coord. Chem. Rev.* **2020**, *406*, 213145. [CrossRef]
65. Wang, J.-X.; Yin, J.; Shekhah, O.; Bakr, O.M.; Eddaoudi, M.; Mohammed, O.F. Energy Transfer in Metal–Organic Frameworks for Fluorescence Sensing. *ACS Appl. Mater. Interfaces* **2022**, *14*, 9970–9986. [CrossRef] [PubMed]